

**In Situ Synthesis and In Operando NMR Studies of High-Performance Ni₅P₄-Nanosheet Anode**

Journal:	<i>Journal of Materials Chemistry A</i>
Manuscript ID	TA-ART-06-2018-005433.R1
Article Type:	Paper
Date Submitted by the Author:	10-Aug-2018
Complete List of Authors:	Feng, Xuyong; Florida State University, Chemistry and Biochemistry Tang, Mingxue; Florida State University, Chemistry O'Neill, Sean; Florida State University, Chemistry Hu, Yan-Yan; Florida State University, Chemistry and Biochemistry



ARTICLE

In Situ Synthesis and *In Operando* NMR Studies of High-Performance Ni₅P₄-Nanosheet Anode

Xuyong Feng,^{†a} Mingxue Tang,^{†ab} Sean O'Neill,^a and Yan-Yan Hu^{*ab}

Received 00th January 20xx,
Accepted 00th January 20xx

DOI: 10.1039/x0xx00000x

www.rsc.org/

Nickel phosphide (Ni₅P₄) nanosheets are synthesized using *in situ* chemical vapor deposition of P on Ni foam. The thickness of the as-synthesized Ni₅P₄ film is determined to be ~5 nm, using atomic force microscopy (AFM). The small thickness shortens the diffusion path of Li ions and results in fast ion transport. In addition, the 2D Ni₅P₄ nanosheets seamlessly connect to the Ni foam, which facilitates electron transfer between Ni₅P₄ and Ni current collector. Therefore, the binder/carbon free-nickel supported Ni₅P₄ shows fast rate performance as an anode for lithium-ion batteries (LIBs). The specific capacity of 2D Ni₅P₄ is obtained as 600 mAh/g at a cycling rate of 0.1 C, approaching the theoretical capacity of 768 mAh/g. Even at a rate of 0.5 C, the capacity remains as 450 mAh/g over 100 cycles. A capacity of >100 mAh/g is retained at a very high rate of 20 C. Ni₅P₄ also exhibits a low voltage of ~0.5 V with respect to Li metal, which makes it a suitable negative electrode for LIBs. *In operando* ³¹P and ⁷Li NMR are employed to probe the lithiation and delithiation mechanisms upon electrochemical cycling.

Introduction

Rechargeable Li-ion batteries (LIBs) have been widely utilized in various portable devices and brought tremendous convenience to our daily life.¹ Searching for safe electrode materials with high energy and power densities is the focus of both fundamental and applied research in recent years.² Electric vehicles require LIBs with high energy density and fast charging capability. Although Li metal anode shows high capacity and low voltage, it is limited for commercial use due to dendrite formation, leading to short circuit of batteries.³ Graphite has been widely employed as the anode in most commercial LIBs but is limited by its low capacity (372 mAh/g or 840 mAh/cm³). Additionally, Li dendrite is found to form on the surface of graphite during battery operation.^{3,4} To overcome these challenges, new and safe anode materials with high energy and power densities are pursued in the past decade. Among these anode candidates, phosphorus (P) and phosphides with high capacity (2594 mAh/g based on P) are

considered as promising anode candidates.^{1,5–15} The potential of P-based anodes (~0.8 V) lies between that of Li₄Ti₅O₁₂ (1.55 V) and of graphite (0.1 V). 0.8-V is a desirable potential for anodes in order to avoid the formation of dendritic lithium and meanwhile offer a higher voltage (compared to Li₄Ti₅O₁₂ anode) when assembled in full batteries.

The high capacity of phosphorus and phosphides originates from multi-electron reactions upon lithiation to form Li₃P, or Li-Ni-P ternary compound. Among phosphorus anodes, red P suffers from poor chemical stability and extremely low electronic conductivity (1 × 10⁻¹⁴ S/cm). Black P is limited by its low electronic conductivity and high cost. To achieve fast rate performance, the anode materials are ideally ion and electron mixed conductors. To enhance electronic conductivity of phosphorous, significant progresses have been made by combining P with different conductive carbon (C)-based materials or synthesizing phosphides. High-energy mechanical milling is one of the common techniques for preparing high performance P/C or phosphide anode materials. Park and co-workers transformed amorphous red P into orthorhombic black P at ambient temperature and pressure. The obtained black P delivered a reversible capacity of 1814 mAh/g with a columbic efficiency of ~90% in the working voltage range of

^aDepartment of Chemistry and Biochemistry, Florida State University, Tallahassee, FL 32306, USA. Email: hu@chem.fsu.edu

^bNational High Magnetic Field Laboratory, 1768 East Paul Dirac Drive, Tallahassee, FL 32310, USA.

[†]These two authors contributed equally and their names are listed in alphabetical order.

Electronic Supplementary Information (ESI) available. See DOI: 10.1039/x0xx00000x

0–2 V.⁷ The P/C composite obtained with the high energy ball milling method shows small particle size with fast rate performance.^{7,16} In addition to carbon, metals such as Sn, Ti, Mo, and Cu are used with high energy mechanical milling in order to improve electrochemical performance. Alternately, P/C composites and phosphides can be obtained via thermal reaction processes. Red phosphorus sublimates at around 450 °C, and adsorbs onto the surface of porous carbon to improve the contact between P and C. This facilitates electron transfer and therefore improves electrochemical performance.^{17–19}

In this contribution, we employ a new protocol to synthesize Ni₅P₄ using chemical vapor deposition (CVD) of P onto the surface of Ni foam. The *in situ* synthesized Ni-foam supported Ni₅P₄ shows 2D nanosheet morphology with large interfacial area, allowing Li ions quickly diffuse. In addition, the close contact between Ni₅P₄ and Ni foam minimizes the resistance for electron transfer. The mixed fast Li-ion and electron transfer of Ni-supported Ni₅P₄ nanosheet accounts for the observed fast rate performance when Ni/Ni₅P₄ is used as anodes in LIBs. *In operando* ⁷Li and ³¹P solid-state NMR are employed to follow the structural and compositional evolution of Ni₅P₄ during electrochemical cycling. The results provide new insights into the lithiation and de-lithiation mechanisms of Ni₅P₄ anodes.

Experimental section

Material synthesis

Nickel phosphide was prepared by using *in situ* chemical growth of P on Ni foam surface. Nickel foam was first cut into small pieces (1 cm x 1 cm) and immersed in 5 M HCl solution for 5 min to eliminate surface oxides. The Ni pieces were then washed with deionized water several times to remove residual HCl. Acetone was used to further wash the treated Ni foam, which was dried in vacuum afterwards. For *in situ* growth of nickel phosphide, about 0.2 g red phosphorus was placed 5 cm away from the Ni foam in an alumina crucible. The Al crucible was then put into a tube furnace and purged with Ar gas for 30 min to remove air before heating. The furnace was heated to 500 °C at a heating rate of 5 °C/min, and then kept at 500 °C for an additional 10 minutes to ensure that the reaction is complete. The furnace was then naturally cooled down to room temperature. During the entire process, Ar gas was fed at a constant rate of ~1 cm³/min and the red phosphorus was placed upstream

relative to the Ni foam. The obtained foam was washed with deionized water and acetone, and then dried under vacuum.

Material characterizations

The structure, chemical phase, and morphology of the as-synthesized nickel phosphide were examined by using powder X-ray diffraction (XRD), scanning electron microscopy (SEM), atomic force microscopy (AFM), X-ray photoelectron spectroscopy (XPS), and solid-state nuclear magnetic resonance (NMR). The Ni-supported Ni₅P₄ was peeled from Ni foam and sonicated in ethanol before XRD, AFM, and NMR measurements.

Powder XRD

Powder XRD patterns were recorded on a X'PERT Pro MPD diffractometer (PANalytical) at 45 kV and 40 mA (Cu K α radiation, $\lambda=0.15406$ nm). Data were collected in the 2 θ range from 10° to 70°, with a scan rate of 6°/min.

SEM

SEM images of the as-synthesized Ni₅P₄ were acquired on a NOVA NanoSEM 400 field-emission scanning electron microscope with different magnifications.

AFM

The AFM experiments were performed on an MFP-3D AFM equipped with an ARC2 controller. To prepare for the AFM characterization, Ni₅P₄ was dispersed in ethanol and sonicated for 30 min, then the Ni₅P₄ suspension was coated on a flat glass and dried at room temperature. The data was analysed using NanoScope Analysis 1.5.

XPS

The XPS measurements were performed using a PHI 5000 series spectrometer. XPS spectra were collected at room temperature using a non-monochromatic (Al K α at 1486.6 eV) X-ray source operated at 400 W, and the chamber pressure was kept below 10⁻⁸ Torr during the measurements. The energy of the spectra was calibrated using the binding energy of the adventitious carbon at 285.0 eV. Data analysis was performed using the CasaXPS software package (version 2.3.18PR1.0). Charge correction was carried out relative to the signal of adventitious carbon (284.8 eV) and a Shirley background model was used. The XPS spectra were fitted using a Gaussian/Lorentzian function (70/30).

In operando solid-state NMR

To prepare for *in operando* NMR characterizations, the as-synthesized material was first grounded and the unreacted nickel metal was removed with a magnet. The purified nickel phosphide was mixed with polyvinylidene fluoride (PVDF, Kynar Flex 2801 from Arkema) and conductive acetylene black (70:10:20 in w/w/w). The mixture was dispersed in N-Methyl-2-pyrrolidone (NMP) and manually grounded in an agate mortar for 30 minutes to form a homogenous slurry. The slurry was cast onto a Ti mesh and dried at 120 °C for 4 hours under vacuum, which was subsequently used as electrodes. The plastic bag cells were assembled using Li and Ni₅P₄ as electrodes and 1 M LiPF₆ in EC/DMC/DEC (w/w=1:1:1) as the electrolyte in an Argon-filled glove-box.

The bag cells were electrochemically cycled inside a home-built static NMR probe. ³¹P NMR spectra were collected while the batteries were cycled at a rate of C/20, assuming the theoretical capacity C=768 mAh·g⁻¹. All *in operando* ³¹P NMR acquisitions were carried out on a Bruker Avance I spectrometer in a 9.4 T magnetic field with a ³¹P Larmor frequency of 161.4 MHz. The ³¹P spectra were obtained using a spin echo sequence with a 90° pulse length of 2.5 μs. 6 k transitions were acquired for each spectrum with a recycle delay of 0.5 s. To accommodate the broad spectra width spanning ~3000 ppm, the ³¹P on-resonance was set on the Ni₅P₄ peak centred at 1400 ppm and the Li₃P peak next to 0 ppm alternately every hour during battery operation. *In operando* ⁷Li NMR spectra were recorded by employing a similar procedure. The acquired NMR spectra were fitted and analyzed by using the Dmfit software.²⁰

Electrochemical tests

The obtained nickel phosphide (Ni₅P₄) supported on the nickel foam was directly used as a working electrode. Lithium metal was used as the counter electrode. The two electrodes were separated with a microporous membrane (Celgard, 2320), soaked with the electrolyte of 1 M LiPF₆ in EC/DMC/DEC (w/w=1:1:1). Coin-type battery cells were assembled in an Argon-filled glove-box (MBraun). The electrochemistry tests were performed on a multi-channel battery test system (LAND) within a voltage range of 0.01 V to 2.0 V. The AC impedance was measured at room temperature on a Reference 600+ Gamry Instrument, within a frequency range from 0.1 Hz to 5×10⁶ Hz.

Results and discussion

During the *in situ* synthesis, the red phosphorus positioned at the upstream side in the furnace sublimates upon increasing temperature, spreads to the nickel foam, and

reacts with nickel to form nickel phosphide. Uniform nanosheet phosphides on the surface of nickel foam is obtained. The SEM images of the nanosheets are shown in Fig. 1. The *in situ* formed nickel phosphide attaches tightly to the nickel substrate (Fig. 1a), which allows electrons to transfer smoothly between nickel phosphide electrode and Ni current collector. This close contact is beneficial to high rate performance. The SEM image in Fig. 1b reveals the formation of uniform and ultrathin nickel phosphide sheets. The thickness of the nanosheets is determined by AFM (Fig. 1c and d). The quantitative analysis of the AFM data shows a very narrow distribution of ~5 nm in thickness (Fig. 1d). The small thickness promotes fast Li-ion transport due to a short diffusion path. Various nickel phosphides (Ni₅P₄, NiP₂ etc.) possibly coexist under different reaction temperatures, time, and molar ratios of P/Ni. In this study, the phase determined to be Ni₅P₄ based on both powder X-ray diffraction (Fig. S1) and ³¹P NMR (Fig. 4) studies²¹ when reactions take place at 500 °C for 10 min. NiP₂ formation is expected with longer reaction time. More heterogenous nanosheets with smaller particles are obtained for the 30 min-treated sample (Fig. S2).

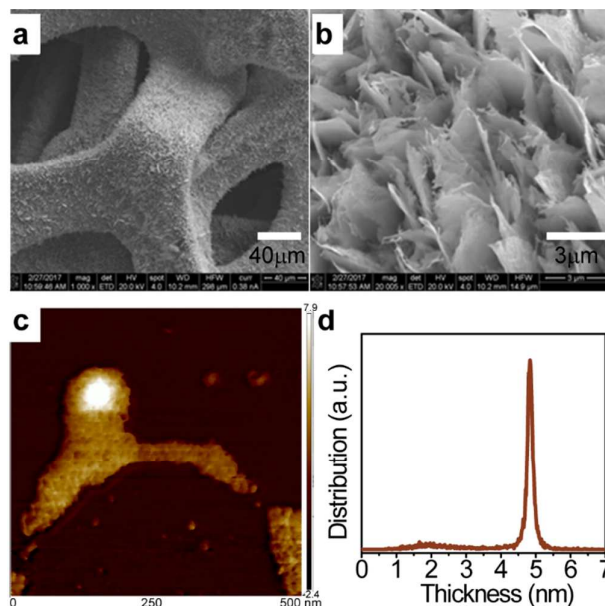


Fig. 1 Microscopic images of the *in situ* synthesized Ni₅P₄ nanosheets supported on Ni foam. (a) and (b) are SEM images with different magnifications of the nickel phosphide on Ni foam, (c) the AFM image, and (d) the histogram of nanosheet thickness obtained from the analysis of AFM results.

The lithiation of nickel phosphide (Ni_5P_4) follows a conversion reaction from Ni_5P_4 to Li_3P and Ni. The calculated theoretical capacity of nickel phosphide is 768 mAh/g. The electrochemical profile of $\text{Ni}_5\text{P}_4/\text{Li}$ half cells for the 1st and 2nd discharge and charge cycles are shown in Fig. 2a. A very steep drop in voltage is observed at the beginning of the 1st discharge from 2.0 to 0.3 V (Fig. 2a), which is rare for phosphides.^{19,22–24} The lithiation between 2.0 V and 0.3 V is attributed to the reaction between NiO on Ni foam and Li, since Ni could be easily oxidized by oxygen (O). Signal related to O_{1s} is observed from the XPS spectrum as shown in Fig. S3. To further support this argument, the following control experiments are performed. Only a small capacity (0.1 mAh for the 1st discharge as shown in Fig. S4) is obtained when NiO is removed by the HCl treatment of the nickel foam. Then the capacity is increased to 0.53 mAh with treatment at 500 °C when minor oxidation occurs during the heating process. The contribution of NiO to the specific capacity in the first discharge is estimated to be about 80 mAh/g (Fig. 2a). The capacity gain between 0.3 V and 0 V is attributed to the conversion reaction from Ni_5P_4 to Li_3P and Ni, and minor formation of solid-electrolyte-interphase. These two processes related to NiO and Ni_5P_4 during the first cycle manifest in the cyclic voltammetry (Fig. S5), from which two separate cathodic peaks present during the first discharge process. The peak at 1.5 V is the reduction of NiO by Li, which is irreversible and disappears upon further charge and discharge. Upon the first charge, electrochemical activities occur over a broad voltage window between 0–2.0 V. The large over potential of the 1st cycle is attributed to the resistance for both ion and electron transfer in insulating NiO upon discharge and irreversible structural disorder. Due to the removal of NiO and formation of Ni during the 1st discharge, the resistance for both ion and electron transport is significantly reduced, thus the overpotential for the 2nd discharge is much smaller. Two processes occur during the 2nd discharge, with one around 0.5 V and the other below 0.3 V. These are related to the step-wise conversion from Ni_5P_4 to Li_3P , which is discussed later in the paper.

The changes in resistance for charge transfer in the Ni_5P_4 anodes upon electrochemical cycling are investigated using electrochemical impedance spectroscopy (EIS). The EIS spectra of a $\text{Ni}_5\text{P}_4/\text{Li}$ half cell before cycling (labeled as “Pristine”), after 1 cycle, and after 100 cycles are displayed in Fig. 2b, which are analyzed using the equivalent circuit model also shown in Fig. 2b and Tab. S1. The solution resistance R_s is around 5 ohms for the cell at these three stages. The charge transfer resistance R_{ct} is 134.7 ohms for the pristine

cell, and it decreases to 1.43 ohms after the first cycle with very slight increase to 1.56 ohms after 100 cycles. The nearly

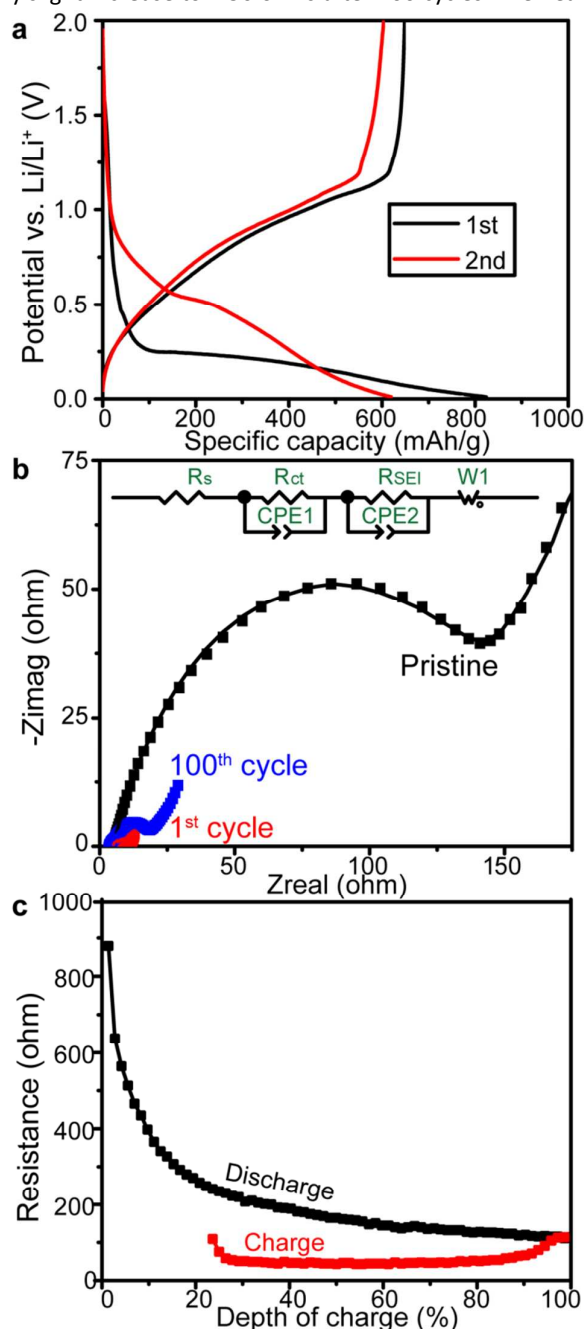


Fig. 2 Electrochemical performance of the Ni_5P_4 anode in $\text{Ni}_5\text{P}_4/\text{Li}$ half cells. a) discharge-charge profile for the first 2 cycles, b) Electrochemical Impedance Spectroscopy (EIS) spectra of a pristine $\text{Ni}_5\text{P}_4/\text{Li}$ battery, and the same battery after the 1st and 100th discharge-charge cycles, and c) DC resistance at different depths of charge during the first discharge-charge cycle, obtained from GITT measurements (Fig. S6).

100-fold drop in charge transfer resistance is probably due to the removal of the insulating NiO on the surface of Ni₅P₄ upon the initial discharge process. As solid-electrolyte-interphases (SEIs) are expected to form upon electrochemical cycling, an additional component in the equivalent circuit model is added to account for their effects on charge transfer in the Ni₅P₄/Li cell after 1 cycle and 100 cycles. The calculated resistance values for charge transfer within the SEIs are 4.35 ohms and 12.55 ohms for the cell after 1 cycle and 100 cycles, respectively.

DC resistance is also measured using the galvanostatic intermittent titration technique (GITT), offering additional insights into the over-potential (Fig. 2c). The electronic resistance for the pristine Ni₅P₄/Li cell is 900 ohms, which gradually reduces to around 100 ohms during the first discharge. Then the electronic resistance continues to decrease at the beginning of the 1st charge and remains around 50 ohms upon further charge. Towards the end of charge, the resistance increases slightly to 100 ohms. The first drop in electronic resistance from 900 to 100 ohms is due to the removal of insulating NiO and the formation of conductive Ni. The small reduction from 100 to 50 ohms at the beginning of the first charge is attributed to the decomposition of resistive SEI. The resistance increase at the end of charge from 50 to 100 ohms is due to the formation of SEI at high voltage. Both ³¹P and ⁷Li NMR suggest SEI formation, which is discussed later.

The rate performance of Ni₅P₄ as anode is studied. A reversible capacity ~600 mAh/g can be achieved at a rate of 0.1 C. Fast cycling rate produces smaller capacity. As shown in Fig. 3, the capacity decreases from 600 to 451 mAh/g when the rate increases from 0.1 C to 0.5 C. Keeping the rate of discharge to be 0.5 C and increasing the charge rate gradually to 20 C, the capacity decreases to 112 mAh/g. When the charge rate is set to 0.5 C again, a capacity of 400 mAh/g is obtained (Fig. 3c), indicating the long-term reversible performance of Ni₅P₄. The columbic efficiency of the first cycle is around 80%, which is higher than typical oxide anodes.²⁵ Almost 100% columbic efficiency is obtained for the subsequent 100 cycles.

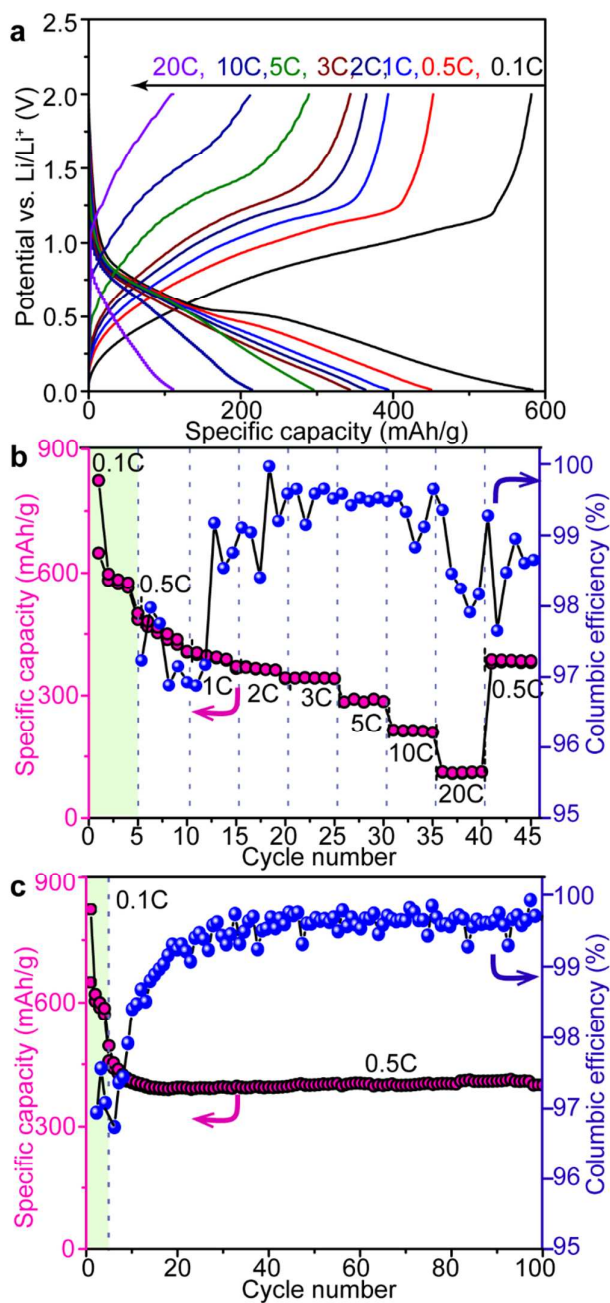


Fig. 3 The rate performance of the Ni₅P₄: a) discharge-charge profiles at different cycling rates. b) the specific capacity as a function of rate, and c) the high-rate performance over extended cycling.

In order to probe the lithiation and de-lithiation mechanism of Ni₅P₄, *in operando* characterizations are performed. For most phosphide anodes, their structures undergo disordering upon discharge-charge cycling process, which makes it difficult to determine with regular microscopic or diffraction tools. Solid-state NMR has been

proven to be a powerful tool to determine the short-range structures of disordered materials.^{26–29} In this contribution, *in operando* ^{31}P and ^7Li NMR spectroscopy are employed to follow the evolution of (de)lithiation of Ni_5P during charge-discharge processes. The structure of Ni_5P_4 is shown in Fig. 4a, in which P is coordinated to various numbers of Ni. P coordinated with 1, 5, 7, and 9 Ni atoms are denoted as P1, P5, P7, and P9. The ^{31}P NMR spectrum of the pristine anode Ni_5P_4 spans over 1500 ppm (500 to 2000 ppm) with the most intense signal at ~ 1700 ppm (Fig. 4b). The ^{31}P shift away from 0 ppm is called Knight shift, a result of the interactions between P spins and conductive electrons. Large Knight shift is observed for Ni_5P_4 compared with that of Cu_3P [~ 400 ppm], which is mainly due to the decrease of *d*-band contribution to the density of states (DOS) at the Fermi level.³⁰ The ^{31}P shift is highly dependent on the number of Ni

locating in the vicinity of P atoms.^{21,30} Five ^{31}P resonances are observed based on spectral analysis shown in Fig. 4b: peak at 1895 ppm is assigned to P9 surrounded 9 Ni, 1670 ppm for P7 surrounded by 7 Ni, 1247 ppm for P5 close to 5 Ni, and the last two peaks at 763 ppm and 720 ppm are assigned as P1 (P next to 1 Ni) and P1' (distorted configuration). It's worth mentioning that the shift is not linearly proportional to the number of nearby Ni because of different bond lengths and angles, which affect spin density transfer (Fig. 4a and top of Fig. 4b). In the middle of the 1st discharge, the four resonances are still visible. P1 shows the largest reduction compared to P5, P7, and P9 (Fig. 4c). At the end of the 1st cycle, the resonances become significantly overlapped compared with the pristine spectrum (Fig. 4d) due to increased structural disorder.

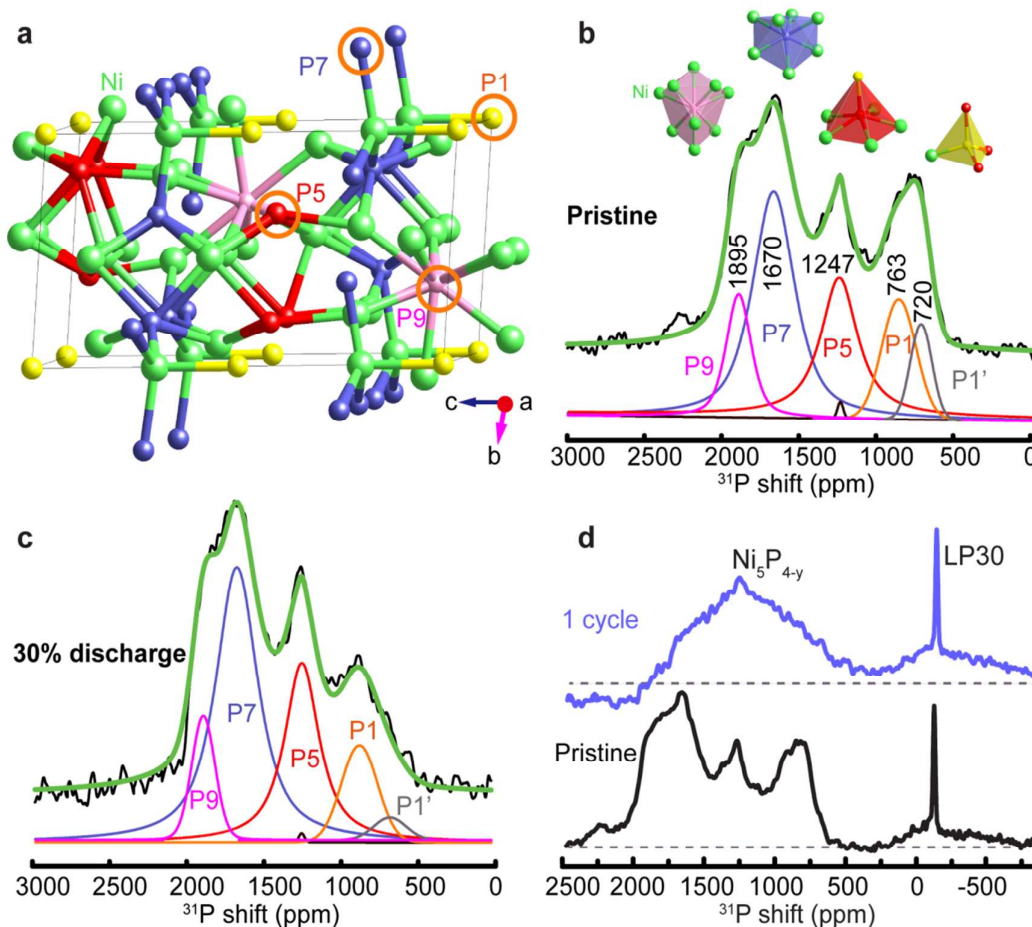


Fig. 4 The structure of Ni_5P_4 and the representative *in operando* ^{31}P solid-state NMR spectra. a) the structure of Ni_5P_4 ; P1, P5, P7, and P9 are phosphorus sites coordinated with 1, 5, 7, and 9 Ni atoms (green), respectively. b) and c) the ^{31}P spectra and the corresponding spectral simulation of the pristine Ni_5P_4 anode and the anode at 50% discharge, respectively. d) the spectral comparison of a $\text{Ni}_5\text{P}_4//\text{Li}$ battery at the pristine state and at the end of the 1st discharge-charge cycle.

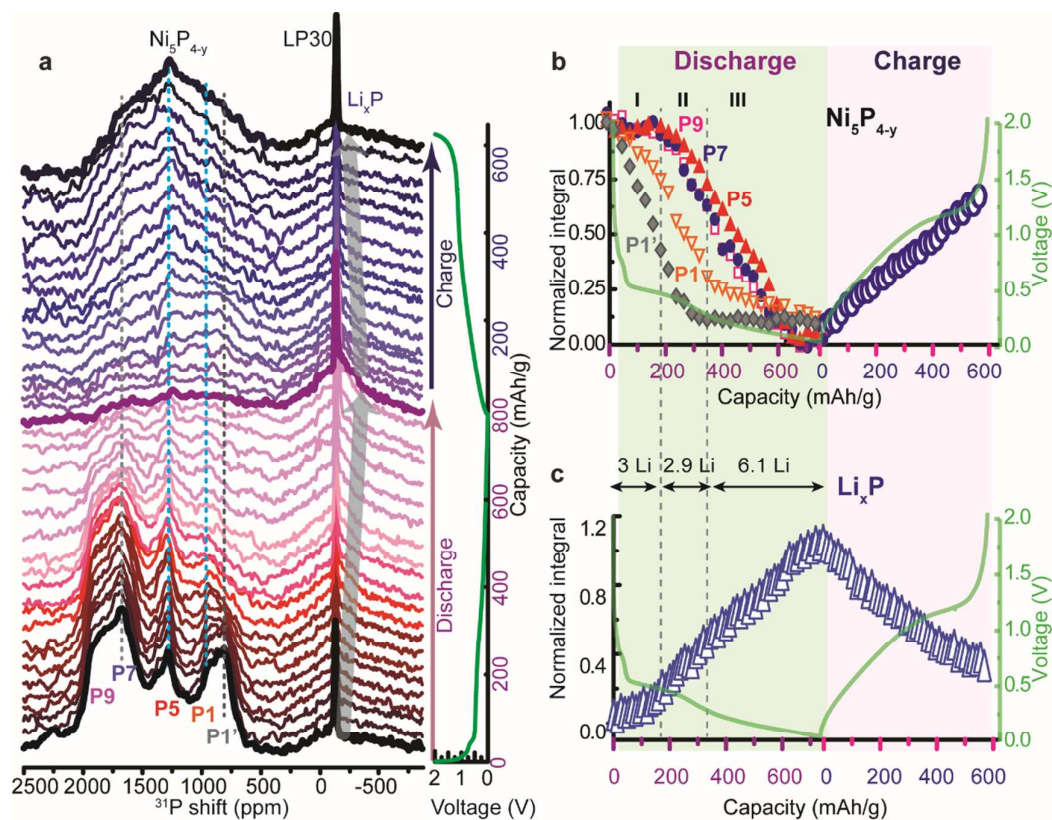


Fig. 5 a) *In operando* ^{31}P NMR spectra of a $\text{Ni}_5\text{P}_4//\text{Li}$ half-cell battery during the 1st cycle and the corresponding electrochemical profile. b) and c) Normalized area integrals of ^{31}P NMR resonances from $\text{Ni}_5\text{P}_{4-y}$ and Li_xP , respectively.

To follow the structural evolution in real time, *in operando* ^{31}P spectra are acquired and shown with the corresponding electrochemical profile in Fig. 5a. In the ^{31}P NMR spectrum of the pristine battery, one additional sharp peak at -140 ppm is observed from electrolyte LiPF_6 as shown in the bottom of Fig. 5a. Upon discharge, Li is stripped from Li anode and inserted into Ni_5P_4 to form $\text{Ni}_5\text{P}_{4-y}$ and Li_3P ; The ^{31}P resonance for Li_3P mainly appears at around -200 ppm. Most P in Ni_5P_4 converts to Li_3P upon further discharge, and the ^{31}P signal of Ni_5P_4 disappears completely at the end of discharge. ^{31}P signal of Li_3P simultaneously grows upon discharge. A recycle delay of 0.5 s is used for the NMR acquisition to optimize for temporal resolution, which is sufficient for $\text{Ni}_5\text{P}_{4-y}$ ($T_1=0.5$ ms) to fully relax, but very short for Li_3P ($T_1=60$ s), therefore the ^{31}P spectra are not quantitative representation of Li_3P . Upon charge, P is released from Li_3P and combined with Ni. Meanwhile, Li is extracted from Li_3P and deposited on Li anode. The original five ^{31}P NMR peaks of Ni_5P_4 become unrecognizable upon charge because the P local structure is

perturbed by Li insertion and extraction and becomes increasingly disordered.

Quantitative analysis is performed on the *in operando* ^{31}P NMR spectra. ^{31}P NMR areal integrals of both $\text{Ni}_5\text{P}_{4-y}$ and Li_xP are shown in Fig. 5b and 5c. The signal of $\text{Ni}_5\text{P}_{4-y}$ shows different reacting rates upon discharge as shown in Fig. 5b. The 1st discharge can be divided into three regions (I, II, and III) by the kink points at ~ 200 mAh/g and ~ 390 mAh/g. At the beginning of discharge (Region I), only P1 and P1' participate in the reaction. The reaction rate of P1' site is much faster than that of P1. P5, P7, and P9, which nearly remain unchanged (or intact) in Region I. P5 starts to take part in the reaction in Region II (190-340 mAh/g) with major reduction in the amount of P7 and P9 sites is observed in Region II. P1 and P1' are reduced to very small amount at the end of Region II and stay intact through Region III (340-750 mAh/g). The major conversion of P5, P7, and P9 sites occur in Region III. The reaction rates of P7 and P9 are almost identical through the entire discharge process. During the 1st charge, all P sites converge to one broad ^{31}P signal centered around

~1500 ppm and the total integral recovers to ~75% of the original, indicating ~25% P is not restored back to $\text{Ni}_5\text{P}_{4-y}$, which is in good agreement with the electrochemical quantification. Accordingly, the signal of Li_3P grows linearly from zero upon lithiation and about 25% remains at the top of charge (Fig. 5c). The *operando* ^{31}P NMR results reveal that the P sites in Ni_5P_4 with fewer Ni coordination convert to Li_3P first at relatively high cell potential compared with reactions to break Ni-P bonds in P5, P7, and P9 configurations. As Gibbs free energy $\Delta G = -nFE$, where n is the number of electron transfer, F is the Faraday constant, and E is the cell potential. $n = 1$ for one-bond breaking of Ni-P, $E_{\text{cell}} = E(\text{cathode}) - E(\text{Li}^+/\text{Li}) = E(\text{cathode}) + 3.4 \text{ V}$. If the cathode reaction occurs at a high potential, it leads to a high cell voltage and thus a large magnitude of Gibbs free energy. It suggests that reactions taking place at a high potential is more spontaneous and require less external energy input than those occurring at a low potential. This finding provides insights into the detailed evolution and reaction thermodynamics of Ni_5P_4 anodes under working condition in real time. It offers a solid explanation at atomic level for the macroscopic observation from electrochemical profiles for nickel phosphides: P coordinated more Ni shows lower average potential vs. Li/Li^+ , e.g. the average potential vs. Li/Li^+ of Ni_5P_4 ³¹ is found to be 0.5 V, which is lower than 0.6 V for NiP_2 .¹⁴

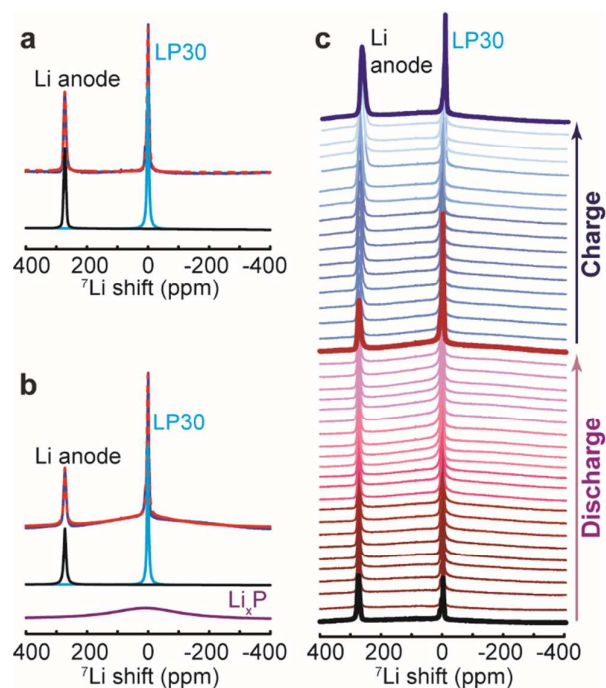


Fig. 6 ^7Li NMR spectra and the corresponding spectral simulation for a pristine (a) and a fully discharged (b)

$\text{Ni}_5\text{P}_4//\text{Li}$ half-cell battery. The experimental spectra are in blue, and the corresponding simulation are in red (dashed lines). The simulated spectra are composed of three components, *i.e.*, Li metal (black line), Li^+ from electrolyte LP30 (grey line), and Li_3P (purple line). (c) Selective *in operando* ^7Li NMR spectra during the first discharge-charge cycle.

In addition to ^{31}P local structural evolution, *operando* ^7Li NMR is performed to follow the dynamics and evolution of (de)lithiation. To achieve this, an identical bag-cell was assembled for the ^7Li NMR study. Two components for the pristine battery are clearly resolved as shown in Fig. 6a. Li anode shows a sharp peak at around 270 ppm.^{14,27} Another sharp peak locating at 0 ppm is attributed to the electrolyte LP30. Upon discharge, Li is stripped from Li anode and inserted into Ni_5P_4 to form Li_3P , of which the ^7Li resonance is at around 0 ppm and the intensity increases upon discharge. Li is electrochemically extracted from Li_3P and then deposits on Li anode upon charge.

Quantitative analysis of the *in operando* ^7Li spectra and the results are shown in Fig. 7. A similar electrochemical profile is obtained compared to the 1st bag-cell battery shown in Fig. 5, indicating good reproducibility. A quick drop of voltage is found at the beginning of the 1st discharge from 2.0 to 0.5 V, and the voltage decreases gradually to zero upon further discharge.

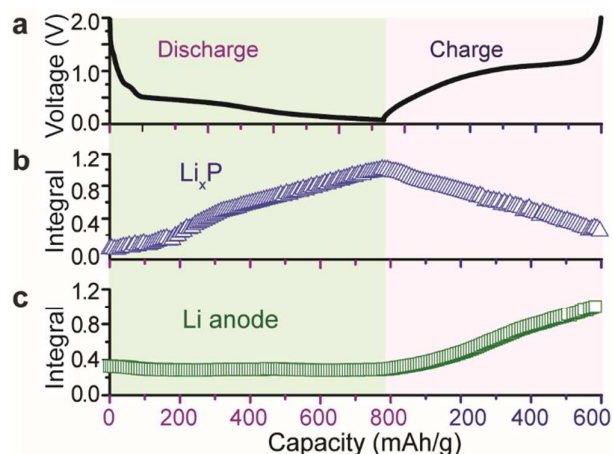


Fig. 7 a) Electrochemical profile of a $\text{Ni}_5\text{P}_4//\text{Li}$ half-cell battery in the working voltage window between 2.0 and 0.0 V. b) and c) Normalized area integrals of the Li_xP and Li resonances from *in operando* ^7Li NMR shown in Fig. 6.

Normalized ^7Li NMR integrals for both Li_3P and Li metal are shown in Fig. 7b and 7c. The signal of Li_3P grows linearly from zero upon discharge. During charge, Li_3P is reversibly converted to Li and $\text{Ni}_5\text{P}_{4-y}$, however about ~25% Li_3P signal

remains at the end of the 1st charge, indicating that ~25% Li remains in Li₃P. It is worth noting that the rate of decrease in the Li₃P amount at the very end of first charge is slowed down, as evidenced by both ³¹P and ⁷Li NMR (Figs. 5 and 7), this is likely due to the formation of SEIs which have overlapped NMR signals around 0 ppm with Li₃P. The Li anode signal remains constant during the 1st discharge, due to skin depth effects.³² However, it grows linearly from zero upon charge due to loose Li microstructures formed on the Li anode surface. In summary, both ⁷Li and ³¹P NMR results consistently illustrate the key modifications of local structures in nickel phosphide upon lithiation and delithiation.

Conclusions

Two-dimensional Ni₅P₄ nanosheets is prepared via *in situ* chemical vapor deposition of red P onto the surface of nickel foam. The structure and morphology of Ni₅P₄ are characterized by XRD, SEM and AFM. Compared with commercial graphite anode, the electrochemical characterizations of the as-synthesized Ni₅P₄ nanosheets show higher capacity, better rate performance, and enhanced long-term cycling stability,^{33–35} making it as a promising anode material for high power Li-ion batteries. The reaction dynamics and local structural modifications of working Ni₅P₄/Li cells are probed by both ⁷Li and ³¹P NMR investigations. *In operando* ³¹P NMR spectra reveal that the ordered Ni₅P₄ becomes amorphous after the 1st cycle. In addition, different P sites are sequentially lithiated; P sites surrounded by fewer Ni react more easily with Li metal than those with more Ni neighbors. Complementary ⁷Li NMR is employed to follow the evolution of Li for both Li anode and Li₃P formed from Ni₅P₄. *In situ* synthesis in conjunction with *in operando* characterizations of nickel phosphide (Ni₅P₄) has led to an anode of fast-rate performance with insights for designing other nickel phosphides.

Conflicts of interest

There are no conflicts to declare.

Acknowledgements

This work is supported by the National Science Foundation under Grant No. DMR-1808517. All the NMR experiments are carried out at the NHMFL, which is funded by the state of Florida and NSF (DMR-1157490).

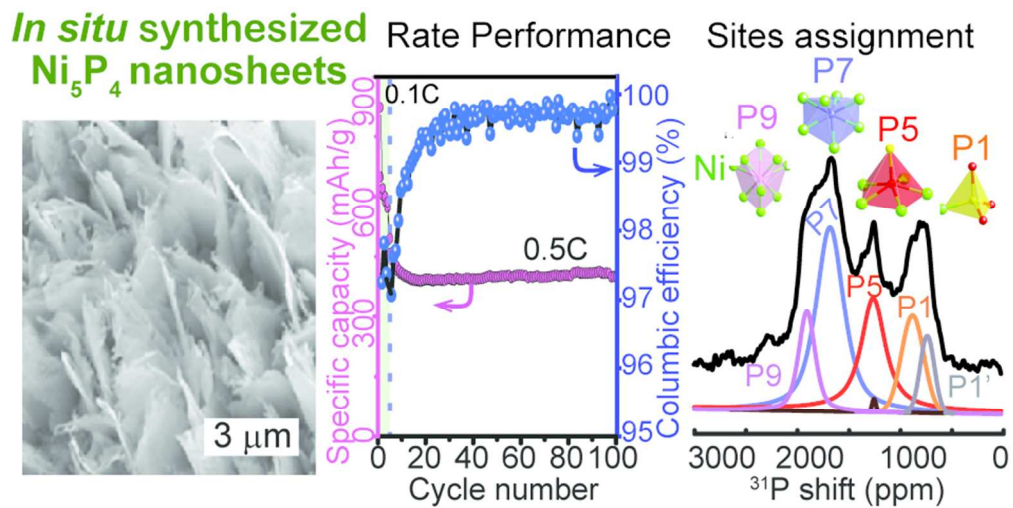
Notes and references

- M. Armand and J.-M. Tarascon, *Nature*, 2008, **451**, 652–657.
- J.-M. Tarascon and M. Armand, *Nature*, 2001, **414**, 359–367.
- W. Xu, J. Wang, F. Ding, X. Chen, E. Nasybulin, Y. Zhang and J.-G. Zhang, *Energy Environ. Sci.*, 2014, **7**, 513–537.
- X. Wang, Z. Na, D. Yin, C. Wang, G. Huang and L. Wang, *Energy Storage Mater.*, 2018, **12**, 103–109.
- F. Gillot, S. Boyanov, L. Dupont, M.-L. Doublet, M. Morcrette, L. Monconduit and J.-M. Tarascon, *Chem. Mater.*, 2005, **17**, 6327–6337.
- H. Hwang, M. G. Kim, Y. Kim, S. W. Martin and J. Cho, *J. Mater. Chem.*, 2007, **17**, 3161.
- C.-M. Park and H.-J. Sohn, *Adv. Mater.*, 2007, **19**, 2465–2468.
- S. Boyanov, J. Bernardi, E. Bekaert, M. Ménétrier, M.-L. Doublet and L. Monconduit, *Chem. Mater.*, 2009, **21**, 298–308.
- C.-M. Park, Y.-U. Kim and H.-J. Sohn, *Chem. Mater.*, 2009, **21**, 5566–5568.
- S. Carencio, D. Portehault, C. Boissière, N. Mézailles and C. Sanchez, *Chem. Rev.*, 2013, **113**, 7981–8065.
- J. Fullenwarth, A. Darwiche, A. Soares, B. Donnadiou and L. Monconduit, *J. Mater. Chem. A*, 2014, **2**, 2050–2059.
- M. Mayo, K. J. Griffith, C. J. Pickard and A. J. Morris, *Chem. Mater.*, 2016, **28**, 2011–2021.
- N. Nitta, D. Lei, H.-R. Jung, D. Gordon, E. Zhao, G. Gresham, J. Cai, I. Luzinov and G. Yushin, *ACS Appl. Mater. Interfaces*, 2016, **8**, 25991–26001.
- P. Lou, Z. Cui, Z. Jia, J. Sun, Y. Tan and X. Guo, *ACS Nano*, 2017, **11**, 3705–3715.
- J. Xu, I.-Y. Jeon, J. Ma, Y. Dou, S.-J. Kim, J.-M. Seo, H. Liu, S. Dou, J.-B. Baek and L. Dai, *Nano Res.*, 2017, **10**, 1268–1281.
- J. Qian, D. Qiao, X. Ai, Y. Cao and H. Yang, *Chem. Commun.*, 2012, **48**, 8931–8933.
- B. Ruan, J. Wang, D. Shi, Y. Xu, S. Chou, H. Liu and J. Wang, *J. Mater. Chem. A*, 2015, **3**, 19011–19017.
- Z. Yu, J. Song, M. L. Gordin, R. Yi, D. Tang and D. Wang, *Adv. Sci.*, 2015, **2**, n/a–n/a.
- W. Li, Z. Yang, M. Li, Y. Jiang, X. Wei, X. Zhong, L. Gu and Y. Yu, *Nano Lett.*, 2016, **16**, 1546–1553.
- D. Massiot, F. Fayon, M. Capron, I. King, S. Le Calvé, B. Alonso, J.-O. Durand, B. Bujoli, Z. Gan and G. Hoatson, *Magn. Reson. Chem.*, 2002, **40**, 70–76.
- E. Bekaert, J. Bernardi, S. Boyanov, L. Monconduit, M.-L. Doublet and M. Ménétrier, *J. Phys. Chem. C*, 2008, **112**, 20481–20490.
- K. Wang, J. Yang, J. Xie, B. Wang and Z. Wen, *Electrochem. Commun.*, 2003, **5**, 480–483.
- M. G. Kim, S. Lee and J. Cho, *J. Electrochem. Soc.*, 2009, **156**, A89.
- J. Tian, Q. Liu, N. Cheng, A. M. Asiri and X. Sun, *Angew. Chem. Int. Ed.*, 2014, **53**, 9577–9581.
- C. Wang, D. Wang, Q. Wang and H. Chen, *J. Power Sources*, 2010, **195**, 7432–7437.
- C. P. Grey and N. Dupré, *Chem. Rev.*, 2004, **104**, 4493–4512.
- R. Bhattacharyya, B. Key, H. Chen, A. S. Best, A. F. Hollenkamp and C. P. Grey, *Nat. Mater.*, 2010, **9**, 504–510.
- J. Zheng, M. Tang and Y.-Y. Hu, *Angew. Chem. Int. Ed.*, 2016, **55**, 12538–12542.
- X. Li, M. Tang, X. Feng, I. Hung, A. Rose, P.-H. Chien, Z. Gan and Y.-Y. Hu, *Chem. Mater.*, 2017, **29**, 8282–8291.
- I. Furo, I. Bakonyi, K. Tompa, E. Zsoldos, I. Heinmaa, M. Alla and E. Lippmaa, *J. Phys. Condens. Matter*, 1990, **2**, 4217.
- J. Jiang, C. Wang, W. Li and Q. Yang, *J. Mater. Chem. A*, 2015, **3**, 23345–23351.

ARTICLE

Journal Name

- 32 A. J. Ilott, S. Chandrashekar, A. Klöckner, H. J. Chang, N. M. Trease, C. P. Grey, L. Greengard and A. Jerschow, *J. Magn. Reson.*, 2014, **245**, 143–149.
- 33 X. Liu, D. Wang, B. Zhang, C. Luan, T. Qin, W. Zhang, D. Wang, X. Shi, T. Deng and W. Zheng, *Electrochimica Acta*, 2018, **268**, 234–240.
- 34 C. E. L. Foss, A. M. Svensson, Ø. Gullbrekken, S. Sunde and F. Vullum-Bruer, *J. Energy Storage*, 2018, **17**, 395–402.
- 35 L. Madec and H. Martinez, *Electrochem. Commun.*, 2018, **90**, 61–64.



80x40mm (300 x 300 DPI)